Available online at www.sciencedirect.com
ScienceDirect
Trans. Nonferrous Met. Soc. China 34(2024) 1864−1877
Transactions of Nonferrous Metals Society of China
www.tnmsc.cn

# Influence of annealing temperature on microstructural evolution and tensile behavior of Ti−6Al−4V alloy manufactured by multi-directional forging

Shi-shuang LIU, Jian-ming CAI, Yi ZHOU, Jing-xia CAO, Wang-feng ZHANG, Sheng-long DAI, Xu HUANG, Chun-xiao CAO

Aviation Key Laboratory of Science and Technology on Advanced Titanium Alloys, AECC Beijing Institute of Aeronautical Materials, Beijing 100095, China

Received 1 January 2023; accepted 1 August 2023

**Abstract:** A range of annealing treatments were implemented to regulate the microstructure and mechanical properties of Ti−6Al−4V forging. The results show that both the as-forged and as-annealed microstructures exhibit a bimodal structure composed of equiaxed primary $\alpha$ phase ($\alpha_p$) and transformed $\beta$ phase ($\beta_t$). With the increase of annealing temperature, the secondary $\alpha$ ($\alpha_s$) phase precipitates from the $\beta$ phase. There is no obvious texture and the crystal orientation is uniformly distributed. Meanwhile, strength initially increases and then decreases, whereas ductility remains largely unaffected. The alloy annealed at 860 °C has an excellent combination of strength and ductility, due to the larger content of the fine $\alpha_s$ phase. All fracture surfaces contain massive dimples, which is a typical ductile fracture feature. The characteristics of microcracks, microvoids, and kinked $\alpha_p/\alpha_l$ (equiaxed $\alpha_p$ and lamellar $\alpha$ phase) phases are found near the fracture.

**Key words:** Ti−6Al−4V forging; annealing temperature; microstructural evolution; secondary $\alpha$ phase; tensile properties; ductile fracture

## 1 Introduction

Owing to low density, high specific strength, and excellent corrosion resistance, titanium alloys are extensively used to manufacture aero-engine components such as fans, compressor disks, and blades [1−3]. Selecting high-performance titanium alloy to replace steel or nickel-based superalloy can reduce the engine weight, raise the thrust-to-weight ratio, and improve the reliability [4].

As a medium strength $\alpha+\beta$ titanium alloy, Ti−6Al−4V alloy can be used up to 400 °C for a long time [5]. The alloy has excellent comprehensive mechanical properties and has drawn considerable attention in the past decades. It is one of the most widely used titanium alloys, and has mature processes, and large application, as the workhorse of $\alpha+\beta$ titanium alloys [6,7]. Generally, Ti−6Al−4V alloy is mainly supplied as bars or forgings, used in mill annealed state, or strengthened by solution and aging treatment. As is well known, titanium alloy can produce various microstructures through different thermal-mechanical histories [8,9]. The microstructural parameters, such as morphology, and size, can affect strength, ductility, and other mechanical properties [10]. Consequently, the microstructure of Ti−6Al−4V alloy can be tailored by thermomechanical processing (TMP) to obtain ideal mechanical properties [11]. Among them, heat

**Corresponding author:** Yi ZHOU, Tel: +86-15210133707, E-mail: ChinaMonday@163.com;
Xu HUANG, Tel: +86-13910936626, E-mail: 13910936626@139.com
DOI: 10.1016/S1003-6326(24)66512-X

treatment is one of the most important approaches to eliminating residual stress, stabilizing micro-structure, and improving mechanical properties. The effect of heat treatment on the microstructural evolution and mechanical behavior of Ti−6Al−4V alloy has been extensively studied. In the case of the same thickness, grains were gradually refined with the decrease in rolling temperature and the dislocation density increased. At the same time, the $\beta$ phase was broken and refined under shear stress, which was beneficial to improving the hardness and strength [12]. Considering the same annealing temperature, a higher cooling rate can refine the microstructure, leading to an increase in the strength, hardness, and fatigue life [13]. Increasing the annealing time from 30 to 120 min does not obviously influence strength, but the ductility constantly decreases. It can be related to the growth of lamellar $\alpha$ thickness [14]. Solution treatment can change the content of constituent phases. The volume fraction of the equiaxed primary $\alpha$ phase decreased with the increase of solution temperature, leading to the improvement of the fatigue crack growth resistance, while the strength increased first and then decreased [15]. JHA et al [16] emphasized that the highest elongation in the equiaxed micro-structure was caused by coarse $\alpha$-lath lamellae and $\alpha'$-lath lamellae, due to the short slip length. LIU et al [17] studied the microstructure and dynamic tensile properties of Ti−6Al−4V alloy processed by selective laser melting (SLM). They found that when the heat treatment was carried out below the $\beta$ phase transition temperature ($T_\beta$), the strength decreased and the ductility increased with the increase of heat treatment temperature. The best properties were obtained at 925 °C in the $\alpha+\beta$ phase region. SINGH et al [10] studied the effect of solution treatment on Ti−6Al−4V alloy produced by extrusion. After $\beta$ quenching and aging treatment, the grains grew up and the microstructure mainly contained metastable martensite $\alpha$ phase. The lamellar microstructure was obtained after quenching and aging treatment in $\alpha+\beta$ phase region. The microstructure and properties of hot isostatically pressed powder Ti−6Al−4V alloy were studied by LU et al [18]. The cooling rate ranged from 5 °C/min to 200 °C/min by jet cooling mode. With the increase of the cooling rate, the transition from $\beta$ phase to $\alpha$ phase became violent. More of the fine lamellar $\alpha$ phases were precipitated in the residual $\beta$ phase, leading to an increase in tensile and fatigue strength. In addition, the deformation temperature and deformation rate can influence the flow stress, microstructure morphology, and phase constitution [19].

It is clear that there have been many previous in-depth researches on the microstructure and mechanical properties of Ti−6Al−4V alloy, with a focus on the influence of equiaxed $\alpha$ phase and lamellar $\alpha$ phase on the properties. However, there are less reports on the effect of the secondary $\alpha$ phase in the transformed $\beta$ phase on tensile properties and fracture mechanism of Ti−6Al−4V alloy. The transformed $\beta$ phase can be adjusted by heat treatments. Among them, annealing treatment has attracted interest as a promising way to improve ductility and stabilize microstructure [5]. Herein, the author took the Ti−6Al−4V forging as the research object, and designed a series of annealing processing to investigate the influence of annealing temperature (in $\alpha+\beta$ phase region) on micro-structure and tensile behavior. Furthermore, the relationship among processing, microstructure, and properties was established. The results in this work will provide new insights for a deeper understanding of the microstructural evolution laws and the regulation of tensile properties for Ti−6Al−4V alloy, so as to broaden its engineering application in aero-engines.

## 2 Experimental

### 2.1 Materials

Ti−6Al−4V alloy ingots were prepared with a triple vacuum arc remelting process. The ingots were cleaned and the surface defects were removed to prevent cracking during the forging process. Then, the alloy was processed by multi-pass multi-directional forging. The multi-directional forging process and sample cutting position are demonstrated in Fig. 1. Firstly, the ingots were forged at 1190 °C, and then forged at 940 °C for multi passes. Eventually, the square billets with the dimension of 100 mm × 100 mm × 1000 mm were obtained. The chemical composition is Ti−6.2Al−4.3V (wt.%).

## 2.2 Heat treatments and tensile tests

The $\alpha+\beta\rightarrow\beta$ transition temperature of Ti−6Al−4V alloy was measured by a conventional metallographic method, and the $\beta$ transition temperature ($T_\beta$) was determined to be about 990 °C. Tensile specimens were machined along the longitudinal direction (LD) of Ti−6Al−4V forging by electrical discharge machining (EDM). All specimens were annealed in the $\alpha+\beta$ phase region, with the annealing temperatures in the range of 780−880 °C, an interval of 20 °C, and a soaking time of 1 h, followed by air cooling (AC). Tensile specimens were processed into $M$12 mm × 71 mm, with a gauge length of $d$5 mm × 25 mm. Standard tensile specimens and analysis samples of TEM, EBSD, and SEM are displayed in Fig. 2. Tensile tests were performed till fracture at room temperature with Instron 5887 tensile machine.

## 2.3 Microstructure and fracture mechanism characterization

Metallographic specimens with the dimension of 10 mm × 10 mm × 10 mm were prepared by rough grinding, fine grinding, mechanical polishing, and chemical etching. Etchant comprises 5% HF, 10% $HNO_3$, and 85% $H_2O$. Microstructure, fracture morphologies, and dislocation structures were characterized by optical microscope (OM, Zeiss), scanning electron microscope (SEM, Sigma 350), electron backscatter diffraction (EBSD, Sigma 350), and transmission electron microscope (TEM, Talos F200 X), respectively. The foils with a thickness of 0.5 mm were cut near the tensile fracture, and then mechanically thinned to 40 μm. TEM samples were prepared by twin-jet polishing using an etchant of perchloric acid, $n$-butanol, and carbinol (with the ratio of 6:34:60). EBSD samples were prepared by vibration polishing method, and the microstructures of initial state, heat treatment state, and longitudinal section of the tensile fracture were observed by means of EBSD. The relationship between crack propagation behavior and microstructure was established by analyzing morphologies of the longitudinal section.

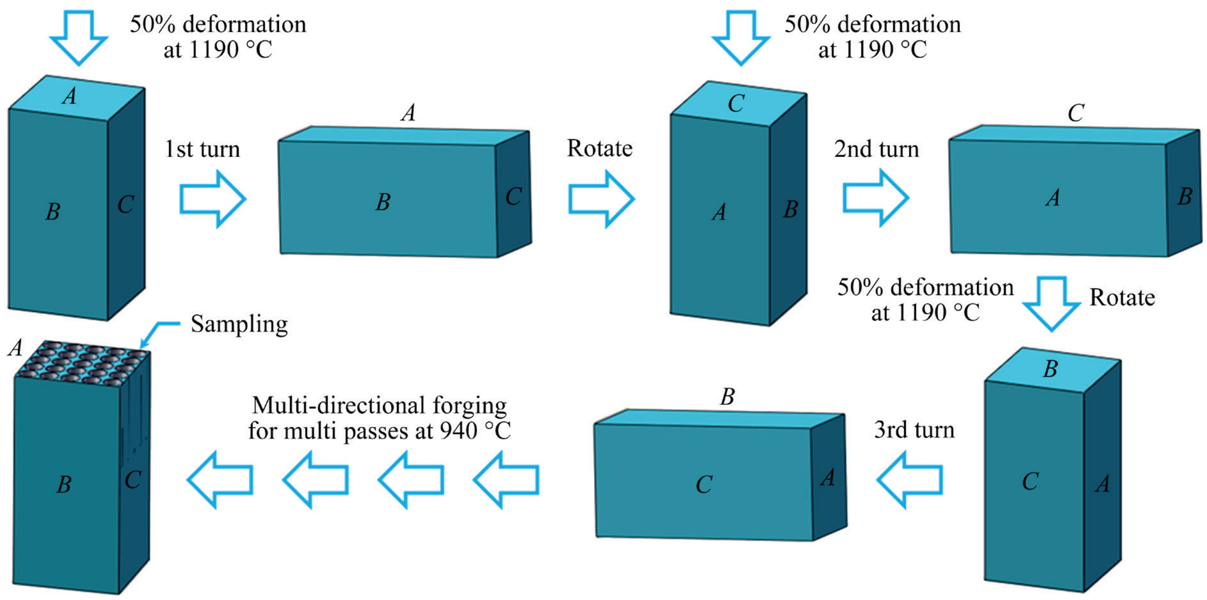


**Fig. 1** Schematic diagram of multi-directional forging process and sample cutting position for Ti−6Al−4V alloy

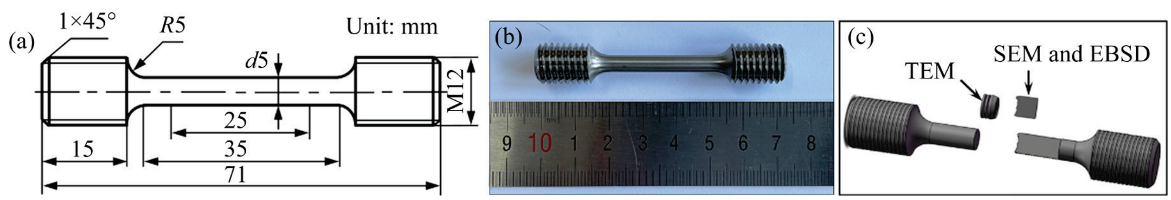


**Fig. 2** Schematic diagram of tensile specimen: (a) Dimension of tensile specimen; (b) Photo of tensile specimen; (c) Analysis samples of TEM, EBSD and SEM

## 3 Results and discussion

### 3.1 Microstructures

The initial microstructure is shown in Fig. 3. It can be seen from Fig. 3(a) that the microstructures in different directions (transverse direction and longitudinal direction are represented by TD and LD) are similar. Figure 3(b) shows the SEM image of the cross-sectional microstructure. Obviously, the as-forged microstructure is a typical bimodal microstructure, composed of equiaxed primary $\alpha$ ($\alpha_p$) phase with an average size of around 15 μm and transformed $\beta$ ($\beta_t$) containing lamellar $\alpha$ ($\alpha_l$) phase. Among them, the equiaxed $\alpha_p$ phases are originated from heavily deformed particles, which are the majority phase of the microstructure and distribute homogeneously throughout the microstructure. It is also proven that the final forging process is in the $\alpha$+$\beta$ phase region. Figure 3(c) shows the inverse pole figures (IPF) image. Different colors in Fig. 3(c) represent different orientations. It can be seen from the IPF image that there is no noticeable texture. And crystal orientation distribution is relatively uniform. The selected area electron diffraction (SAED) patterns in Fig. 3(d) demonstrate that the equiaxed phase, lamellar phase, and matrix phase correspond to $\alpha_p$, $\alpha_l$, and $\beta$ phases, respectively. The results are consistent with SEM images. The element analysis results by energy dispersive spectroscopy (EDS) are given in Table 1. The results indicate that the $\beta$ phase is richer in V and lean in Al than the $\alpha_p$ phase. The difference of V and Al contents in $\alpha$ and $\beta$ phases suggests that alloying element partitioning between the $\alpha$ phase and $\beta$ phase occurs.

**Table 1** Element contents of $\alpha_p$ and $\beta$ phases (wt.%)

| Phase | Ti | Al | V |
|---|---|---|---|
| $\alpha_p$ | 90.79 | 7.39 | 1.82 |
| $\beta$ | 81.98 | 3.97 | 14.05 |

Figure 4 shows the SEM images of the as-annealed microstructure. It is evident that the as-annealed microstructure is similar to the as-forged microstructure, so-called bimodal micro-structure, consisting of equiaxed $\alpha_p$ and $\beta_t$. As can be seen from Fig. 4, the size of the equiaxed $\alpha_p$ phase gradually decreases with the increase of annealing temperature due to high temperature dissolution, which indicates that $\alpha\rightarrow\beta$ phase transition occurs during annealing process [20,21]. But it is difficult for the equiaxed $\alpha_p$ phase to dissolve during the annealing process in the $\alpha$+$\beta$ phase region, only achieving the purpose of stabilizing microstructure. When the annealing temperature is higher than 800 °C, the metastable $\beta$ phase decomposes and transforms into fine $\alpha_s$ phase (Figs. 4(b−f)). While the alloy is annealed at 780 °C, there is no precipitation of $\alpha_s$ phase from $\beta$ (Fig. 4(a)). In the meantime, there is no obvious $\beta$ grain in the microstructure, due to the weak atomic diffusion capacity. The content and the size of the

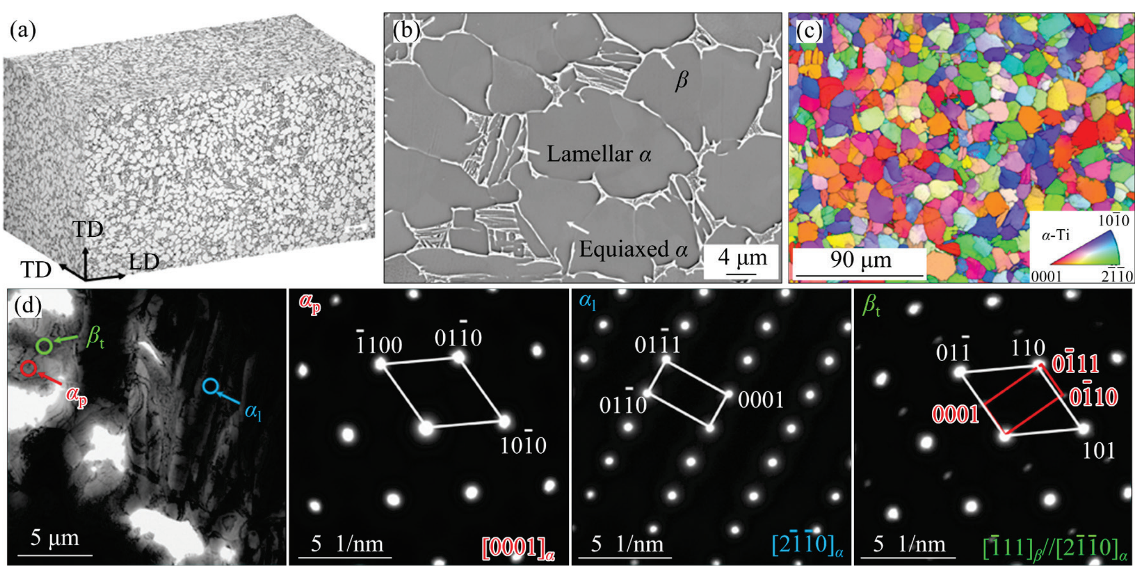


**Fig. 3** Initial microstructures of Ti–6Al–4V alloy: (a) OM images; (b) SEM image; (c) IPF image; (d) Bright-field image and SAED patterns of $\alpha$ and $\beta$ phases

fine $\alpha_s$ phase increase gradually with the increase of annealing temperature. Elemental contents of Al and V in $\alpha_p$ and $\beta_t$ phases are summarized in Table 2, and element mappings of V obtained after different annealing temperatures are shown in Fig. 5. The results show that the Al content in $\beta_t$ phase increases with the increase of annealing temperature, while the V content decreases. Table 2 also indicates that Al and V contents in the $\alpha_p$ phase do not change much. The difference in Al content between the $\alpha_p$ and $\beta_t$ gradually decreases with the increase of annealing temperature, which is consistent with the results of CHONG et al [22]. As to the microstructure annealed at 880 °C, as shown in Fig. 4(f), the content of $\beta_t$ is the largest, which is a result of initial $\beta$ phase expansion and is related to V diffusion during the annealing process [23]. Additionally, the increase of fine $\alpha_s$ phase is directly related to the increase of $\beta_t$ content, and the larger volume fraction is caused by the higher transformation kinetics. The coarsening of the $\alpha_s$ phase is a thermally activated process [24]. Thus, the fine $\alpha_s$ phase coarsens obviously at 880 °C (Fig. 4(f)). Meanwhile, as seen in Figs. 4 and 5, the interface between $\beta_t$ and $\alpha_p$ appears bright, indicating a higher content of V. The precipitation of the fine $\alpha_s$ phase may take place within the $\beta_t$ rather than at the $\alpha_p$/$\beta_t$ interface. It is consistent with the observation in SEM images that no $\alpha_s$ phase is formed at the $\alpha_p$/$\beta_t$ interface. Figure 6 shows the IPF maps of Ti−6Al−4V alloy with annealing treatments at different temperatures. Obviously, it can be found that the microstructures of annealing states have no significant texture, and crystal orientation distribution is random. At the same time, it can be found that a part of the $\alpha_l$ phase is dissolved at a high annealing temperature.

**Table 2** Elemental contents of Al and V in $\alpha_p$ and $\beta_t$ phases (wt.%)

| Temperature/°C | Al | | V | |
|---|---|---|---|---|
| | $\alpha_p$ | $\beta_t$ | $\alpha_p$ | $\beta_t$ |
| 780 | 7.48 | 4.18 | 1.89 | 11.52 |
| 800 | 7.35 | 4.55 | 1.90 | 9.90 |
| 820 | 7.21 | 4.71 | 2.21 | 9.72 |
| 840 | 7.24 | 4.85 | 1.97 | 9.21 |
| 860 | 7.23 | 5.40 | 2.05 | 7.09 |
| 880 | 7.39 | 5.62 | 1.83 | 6.40 |

An important conclusion can be summarized as the content and the size of $\alpha_p$, $\alpha_l$, and $\alpha_s$ phases are affected by annealing temperature. The $\beta\rightarrow\alpha$ transformation process in Ti−6Al−4V alloy can occur through diffusion controlled by a nucleation and growth process [25]. In this study, annealing is performed in the $\alpha$+$\beta$ phase region. When cooled at a high temperature, a higher initial temperature leads to a larger cooling rate, which can induce a higher nucleation rate of the $\alpha_s$ phase [8], so the content and the size of the fine $\alpha_s$ phase increase. The change of the content and the size of $\alpha_p$ and $\alpha_l$ phases are opposite to those of the fine $\alpha_s$ phase. The microstructural evolution of Ti−6Al−4V alloy with different annealing processes is schematically summarized in Fig. 7.

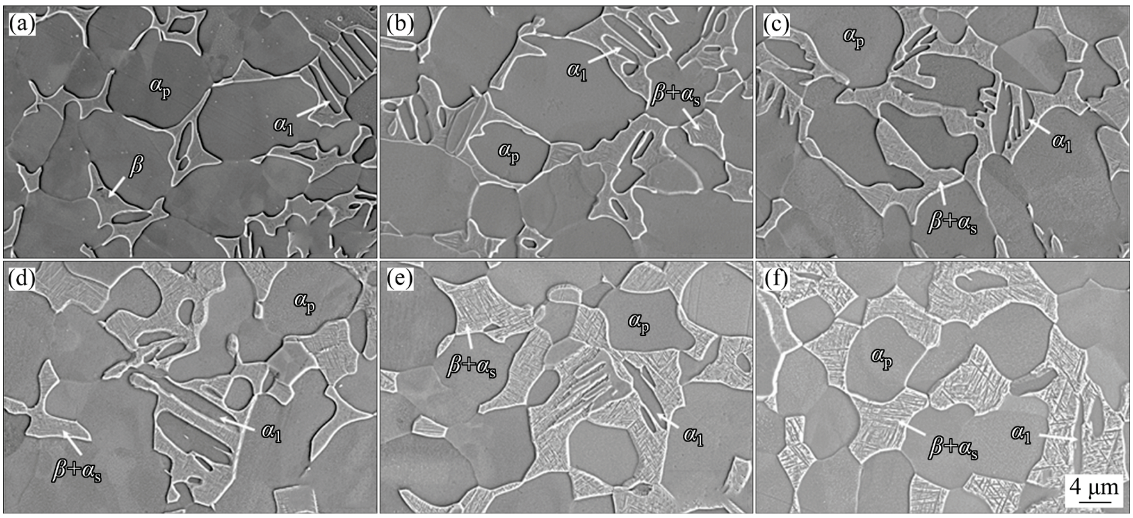


**Fig. 4** Microstructures of Ti−6Al−4V alloy after annealing treatment at different temperatures: (a) 780 °C; (b) 800 °C; (c) 820 °C; (d) 840 °C; (e) 860 °C; (f) 880 °C

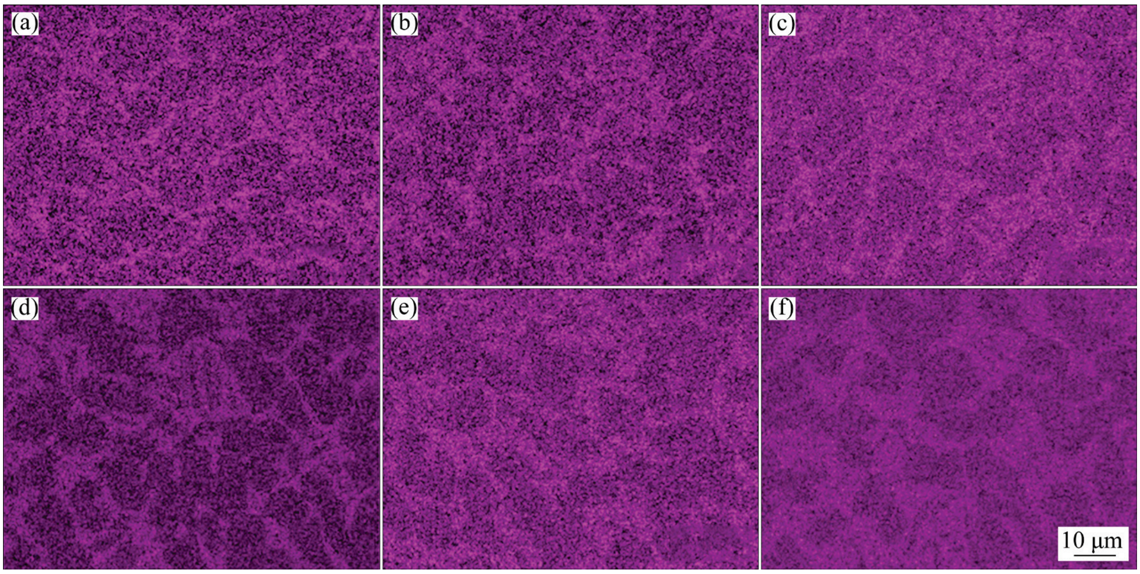


**Fig. 5** Element mappings of V obtained after annealing treatment at different temperatures: (a) 780 °C; (b) 800 °C; (c) 820 °C; (d) 840 °C; (e) 860 °C; (f) 880 °C

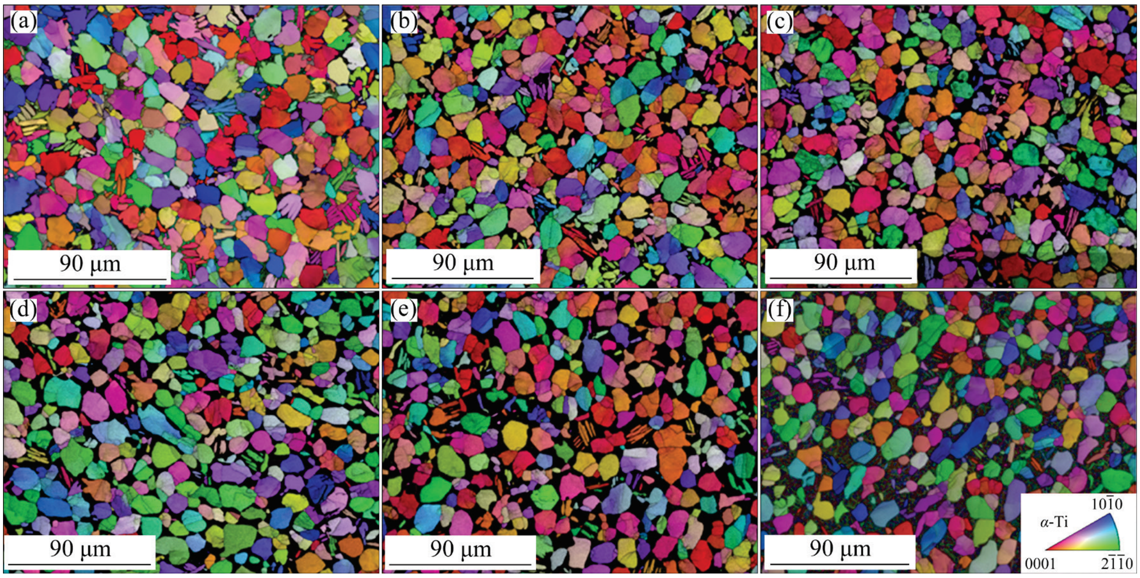


**Fig. 6** IPF maps of Ti−6Al−4V alloy after annealing treatment at different temperatures: (a) 780 °C; (b) 800°C; (c) 820 °C; (d) 840 °C; (e) 860 °C; (f) 880 °C

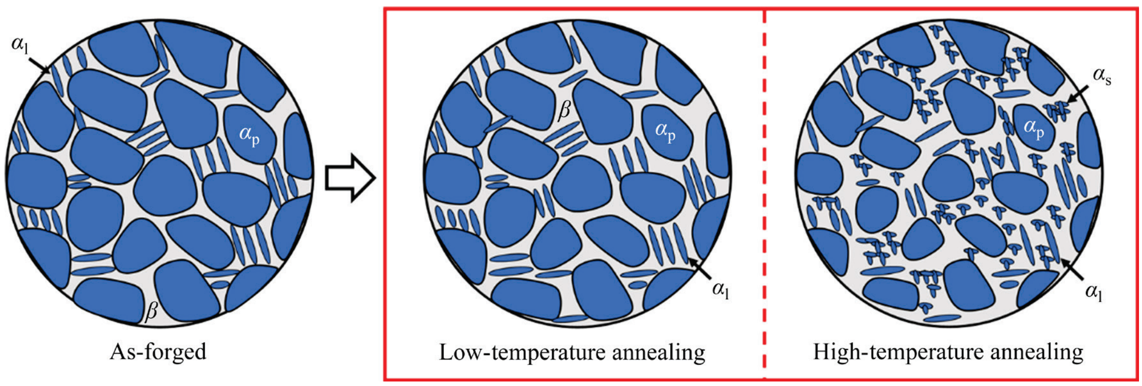


**Fig. 7** Schematic diagram of microstructural evolution for Ti−6Al−4V alloy

### 3.2 Tensile properties

Uniaxial tensile tests were conducted to figure out the effect of annealing temperature on mechanical properties. Figure 8 shows the tensile engineering stress−strain curves of Ti−6Al−4V alloy. All stress−strain curves have similar characteristics, including four typical stages, i.e., elastic stage, yield stage, hardening stage, and necking stage. As presented in the curves, slopes are the same at the elastic stage; that is to say, the elastic modulus is the same. In the hardening stage, work hardening is not obvious, which results from vast dislocation tangle and dislocation multiplication at the deformation stage [26]. Interestingly, when the curves reach the top point, all groups of specimens go through a necking process instead of breaking immediately. The relationship between tensile properties and annealing temperatures is displayed in Fig. 9. The ratio of yield-to-tensile strength is in the range of 85%−92%. The ultimate tensile strength (UTS), yield strength (YS), elongation (EL), and reduction of area (RA) of the unannealed alloy are 955.7, 880.7 MPa, 18.4%, and 50.0%, respectively. The as-annealed alloy reveals the characteristics of high ductility and medium strength. It can be seen from the tendency of tensile curves that an upward trend appears in UTS and YS at an annealing temperature below 860 °C. UTS increases from 983.7 to 1041 MPa and YS increases from 837.3 to 937.7 MPa, which represents a significant improvement of 5.8% and 12.0%, respectively, compared to the annealed state at 780 °C. As the annealing temperature continues to rise to 880 °C, UTS and YS show a slightly downward trend. To sum up, tensile strength increases first and then decreases. Thereby, the annealing temperatures are divided into two regions, that is, Region I (780−860 °C) and Region II (860−880 °C). EL and RA have no apparent fluctuation. EL is above 15.8% and RA is above 44%. Tensile ductility is less affected by annealing temperature. The strength and ductility of Ti−6Al−4V alloy are well matched when annealed at 860 °C, and the average values of UTS, YS, EL, and RA are 1041 MPa, 937.7 MPa, 16.0%, and 45.6%, respectively. Table 3 summarizes the tensile properties of Ti−6Al−4V alloy prepared by different TMPs such as rolling, forging, extrusion, hot isostatic pressing, and wire and arc additive manufacturing. It is evident that Ti−6Al−4V alloy processed by multi-directional forging and annealing treatment has higher strength and better ductility.

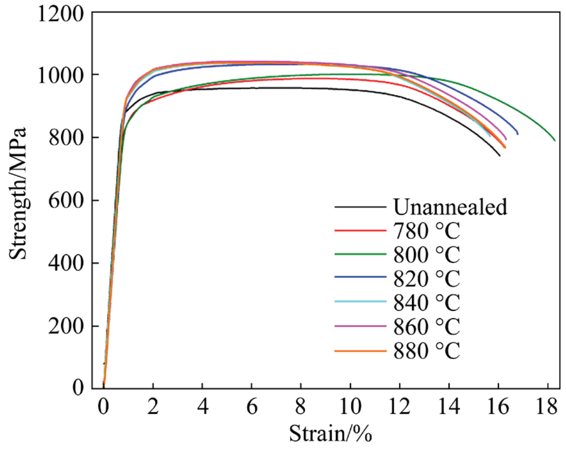


**Fig. 8** Engineering stress−strain curves of Ti−6Al−4V alloy

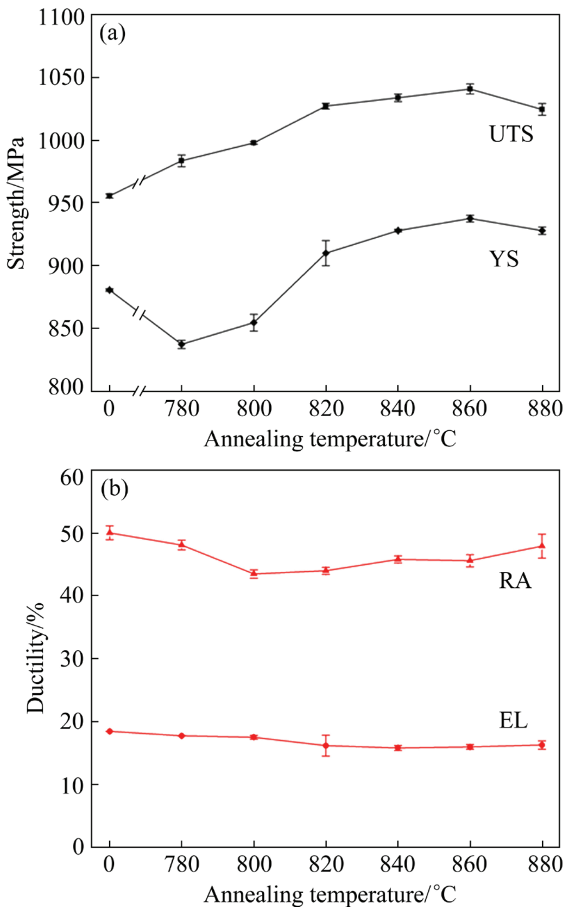


**Fig. 9** Room-temperature tensile properties of Ti−6Al−4V alloy: (a) Strength; (b) Ductility

Through above results, it can be drawn that microstructure morphologies have a significant influence on tensile properties. Although slip in the $\beta$ phase is beneficial to tensile deformation, the

**Table 3** UTS and EL of Ti–6Al–4V alloy treated by different TMPs

| TMP | UTS/MPa | EL/% |
|---|---|---|
| Multi-directional forming and annealing (this work) | 1041 | 16.0 |
| Hot isostatic pressing [27] | 939 | 20.1 |
| Selective laser melting [28] | 1035 | 9.6 |
| Rolling [29] | 1027 | 11.5 |
| Mill annealing [16] | 1019 | 7.8 |
| Rolling [13] | 971 | 6.4 |
| Forging−additive hybrid [30] | 945 | 14.1 |
| Wire and arc additive manufacturing [8] | 1035 | 5.3 |
| Hot isostatic pressing [18] | 980 | 17.0 |
| Extrusion [10] | 1056 | 4.9 |

contribution of very low $\beta$ phase content to the ductility is negligible. So, the majority of ductility is accommodated by the $\alpha$ phase which has limited slip systems [31]. The strength of titanium alloy is closely related to secondary phase precipitation, namely the fine $\alpha_s$ phase precipitation. The larger content of the $\alpha_s$ phase can stabilize microstructure and properties, playing a strengthening role. The competitive relationship between the softening caused by the coarsening of the $\alpha_s$ phase and the strengthening caused by the increase of the fine $\alpha_s$ phase content is the fundamental reason for the initial increase and subsequent decrease in strength [5]. When annealed at 780 °C, the $\alpha_p$ phase content is the highest and the effect of alloying element distribution is the highest. $\beta$ phase is the weaker phase, which will be strengthened by the secondary phase formed in the $\beta$ phase [18]. The strength is the lowest due to the absence of fine $\alpha_s$ phase precipitation in $\beta$ phase. When the annealing temperature increases from 800 to 860 °C, the thermal activation energy of second phase precipitation increases. So, much fine $\alpha_s$ phase is generated in the $\beta$ phase, which can hinder the dislocation movement, playing a strengthening role [18,32]. The strengthening effect of the fine $\alpha_s$ phase is greater than the weakening effect of alloying element distribution. And the precipitation strengthening plays a leading role [5,33]. More fine $\alpha_s$ phase can provide more $\alpha/\beta$ phase interfaces, which can act as obstacles for dislocation slip and inhibit dislocation motion. Simultaneously, these results lead to the shortening of the dislocation slip distance [34]. So, the strength increases. As the annealing temperature rises to 880 °C, the $\alpha_s$ phase obtains sufficient growth driving force, and its content and size increase. The coarsening of the $\alpha_s$ phase leads to a decrease in the number of $\alpha/\beta$ phase boundaries and an increase in the slip distance of dislocation, which can reduce the dislocation slip resistance and weaken the strengthening effect of the $\alpha_s$ phase. Thus, the lower annealing temperature results in a higher strength, which is the same as the conclusion of CHEN et al [35]. Consequently, the size and the number of $\alpha_s$ phase in $\beta$ phase have a great influence on the mechanical properties of Ti–6Al–4V alloy. The dispersed $\alpha_s$ phase not only exhibits relatively high precipitation strengthening effect to improve the strength, but also causes deformation match and deformation compatibility which contribute to a higher ductility [8]. The (860 °C, 1 h, AC) is found to be the best heat treatment in this study.

### 3.3 Fracture behaviors

Representative fractures of the alloy annealed at 780, 820, and 860 °C were selected to analyze fracture morphologies. Figure 10 shows the whole and local fracture morphologies of cross sections. Each subfigure in Figs. 10(a−c) contains three illustrations: (1) macroscopic fractures, (2) amplified images of the crack source region (Position I in macroscopic fracture), and (3) amplified images of shear lip region (Position II in macroscopic fracture). Macroscopic fracture surfaces are rough and cup-cone-shaped. The fracture is silver-gray with a visible necking feature, which conforms to a typical ductile fracture. Fracture surfaces are made up of three regions, i.e., crack initiation region (center rough fiber region), crack propagation region (radiation region), and edge shear lip region. Cracks are initiated in the central fiber region and then propagate to the edge of the specimen. As shown in micro-morphologies, the fracture surfaces have ductile fracture characteristics with numerous dimples of different sizes and shapes. The crack initiation area is formed by shallow and equiaxed dimples. There are secondary cracks in dimples, which can absorb a part of energy. It can reduce the stress concentration during tensile deformation, leading to obtaining high ductility. The shear lip region consists of deeply equiaxed and shear dimples.

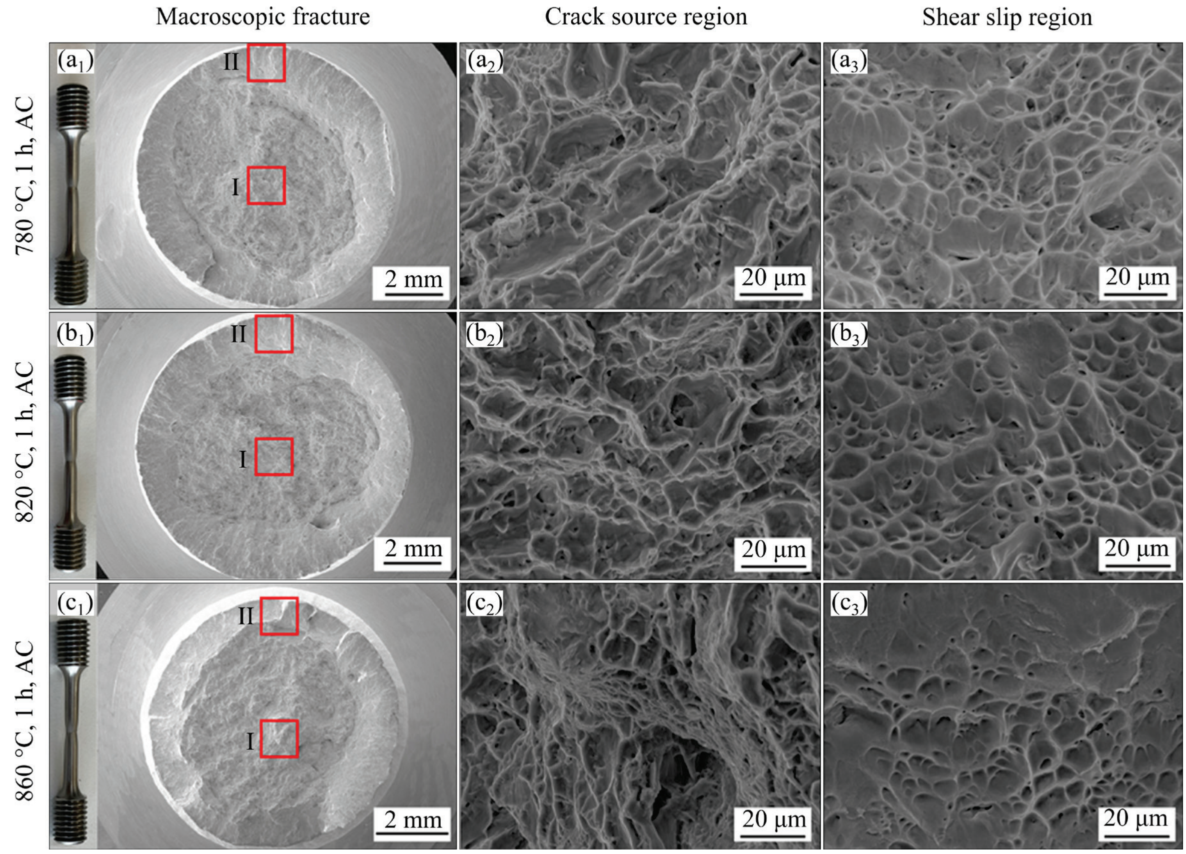


**Fig. 10** Transverse fracture morphologies of tensile specimens annealed at different temperatures: (a) 780 °C; (b) 820 °C; (c) 860 °C

The proportions of the three regions for all tensile fractures are similar, and so does the ductility. Small pores can also be seen in the dimples, which may be caused by strain mismatch between $\alpha_p$ and $\beta$ phases. As mentioned above, fractographies, fracture modes, and stress−strain curves all reveal that as-annealed alloy primarily exhibits a ductile fracture with good ductility.

It should be noted that tensile fractures have the same fracture surface (mode), and so does the fracture mechanism. A representative fractured specimen, annealed at 800 °C, was selected to analyze the microstructure morphologies and crack propagation of the longitudinal section. Figure 11 illustrates the deformed microstructures and crack propagation paths. There are some main characteristics. Micropores are observed in the area of stress concentration [36], i.e., the interior of the $\alpha_p$ phase, which may be induced by unstable necking stage [26]. Microcracks are approximately 45° from the tensile direction (Figs. 11(b, c)), since the principal shearing stress along 45° is the greatest. The cracks propagate across $\alpha_p$ and $\alpha_l$ phases. And it can be clearly seen that equiaxed $\alpha_p$ phases are evidently elongated. Besides, some $\alpha_p$ and $\alpha_l$ phases are kinked towards the tensile direction, indicating that $\alpha_p/\alpha_l$ phases have undergone the large plastic deformation before the final fracture (Fig. 11(c)). The microstructure far away from the fracture is illustrated in Fig. 11(d), showing a slight elongation.

As widely accepted, there are three types of available slip systems with a $\langle 11\bar{2}0\rangle$ Burgers vector ($a$-type), including basal {0001}, prismatic $\{10\bar{1}0\}$, and first-order pyramidal $\{10\bar{1}1\}$ planes [37] Figure 12 depicts the kernel average misorientation (KAM) map, image quality (IQ) map, Schmid factor distribution map, and IPF map. Among them, the KAM map is an indirect measure to represent the arrangement and distribution of dislocations. As observed in the KAM map, the strain accumulation is higher at the $\alpha_p/\beta$ phase interfaces, which can make it easier to form the dislocations and slip bands. The Schmid factor as a relevant indicator of the local plastic activity can determine the favorable slip system [38]. Some dislocation lines (marked with white arrows) are observed within $\alpha_p$ grains (Figs. 12(a−d)). These locations present higher basal or prismatic Schmid factors. This indicates that the basal or prismatic slip system in elongated $\alpha_p$ grains is activated. The value of Schmid factor in prismatic $\langle a\rangle$ slip system is higher than that of basal $\langle a\rangle$ slip system (Figs. 12(c, d)). The higher the Schmid factor is, the easier the slip system is to be activated. This is because the critical resolved shear stress (CRSS) of the prismatic $\langle a\rangle$ slip system is lower than that of the basal $\langle a\rangle$ slip system [38]. The preferential deformation modes in the $\alpha_p$ phase happen on the prismatic and basal slip systems, showing a feature of multiple slips. Crystallographic orientations of cracked $\alpha_p$ grains are presented in Fig. 12(e) and marked by the schematic 3D crystal cell. The orientations of the crack propagation path are random. The cracks cross through the whole $\alpha_p$

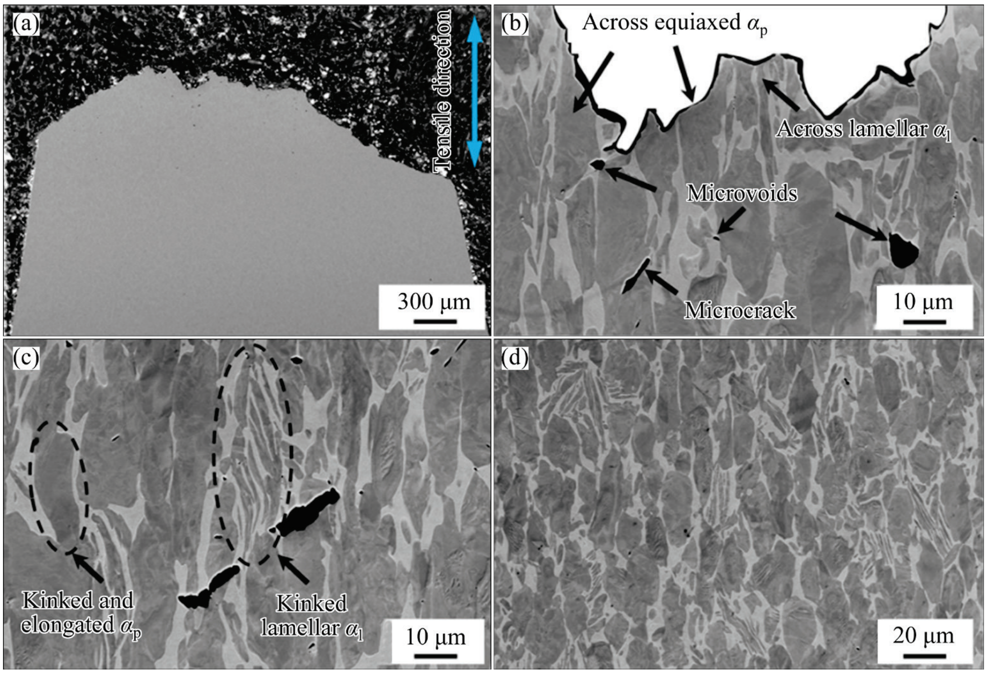


**Fig. 11** Longitudinal fracture morphologies of tensile specimen annealed at 800 °C: (a) Macroscopic morphologies; (b, c) Crack propagation pathways (across equiaxed $\alpha_p$, across lamellar $\alpha_l$, features of elongated $\alpha_p$ and kinked $\alpha_p/\alpha_l$); (d) Microstructure far away from fracture

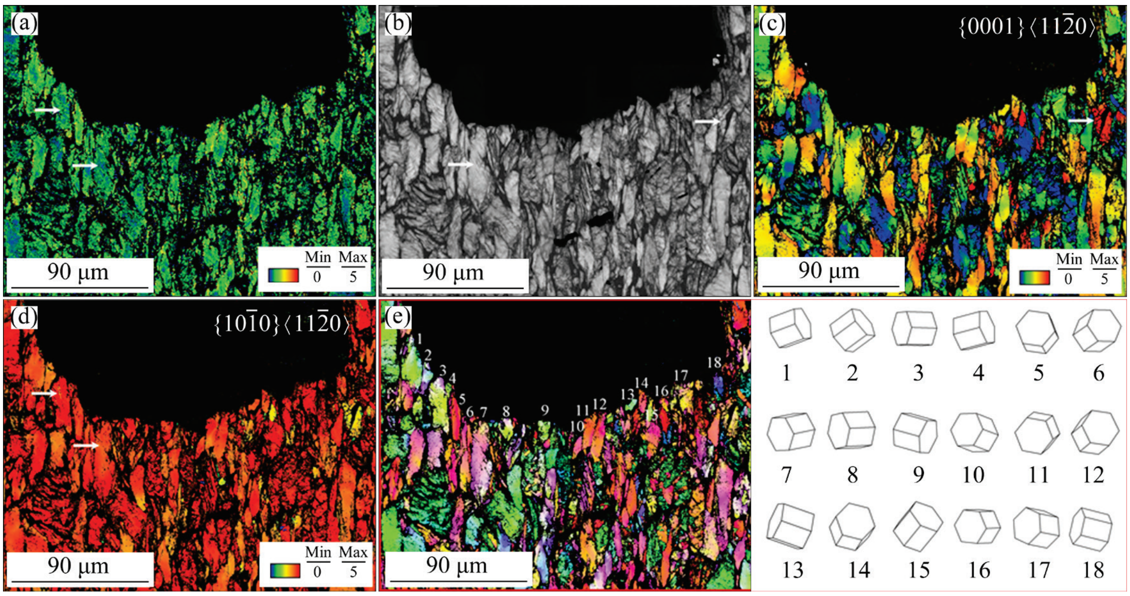


**Fig. 12** EBSD analysis results of longitudinal section of tensile specimen annealed at 800 °C: (a) KAM map; (b) IQ map; (c) Basal slip; (d) Prismatic slip; (e) IPF maps of $\alpha$ phase crack tip by 3D crystal viewer

grains instead of bypassing the grains, which is consistent with the results in Fig. 11.

For further understanding the fracture mechanism, dislocation morphologies of tensile fracture of the alloy annealed at 800 °C were thoroughly investigated by the TEM method. The zone axis $b$ is $[11\bar{2}0]$ and reciprocal lattice vectors (expressed by $g$) are $g$=0002 and $g=10\bar{1}0$, respectively. According to the visible law ($g \cdot b$=0) of dislocation types in $\alpha$ phase, when $g=10\bar{1}0$, $a$-type dislocation is visible; when $g$=0002, $c$-type dislocation is visible, and ($a$+$c$)-type dislocation is visible when $g$=0002 and $g=10\bar{1}0$ [39]. The majority of dislocations are estimated as $a$-type and $c$-type dislocations (Fig. 13). Meantime, it can be found that high-density dislocations were stacked at phase inter-faces (including the interfaces of $\alpha_p/\beta$ and $\alpha_l/\beta$) as well as within the $\beta$ phase. It is clear that the interfaces act as an obstacle to prevent the dislocations from entering the $\alpha$ phase. Most of the mechanical properties are related to the movement/interaction of dislocation [16]. The resistance of dislocation movement is related to the average free path/slip length. In the bimodal microstructure of Ti−6Al−4V alloy, slip length is closely related to the size of $\alpha_p$ and $\alpha_l$ phases. As a result, when the annealing temperature is between 780 and 860 °C, with the increase of annealing temperature, the content of $\alpha_s$ phase increases, leading to the increase of the phase interfaces. These changes can effectively reduce the slip distance of dislocations. The dislocations are pinned at the phase boundaries to hinder the deformation, which makes the strength increase [30]. When annealed at 880 °C, the size of the $\alpha_s$ phase increases, and the resistance to dislocation movement and the strength decrease compared with the alloy annealed at 860 °C.

Based on the aforementioned analysis, including microstructure morphologies, strain distribution, slip system, and dislocation morphologies, a complete picture of the deformation behaviors of bimodal microstructure (from initial micro-structure to fractured microstructure) can be drawn, as illustrated in Fig. 14.

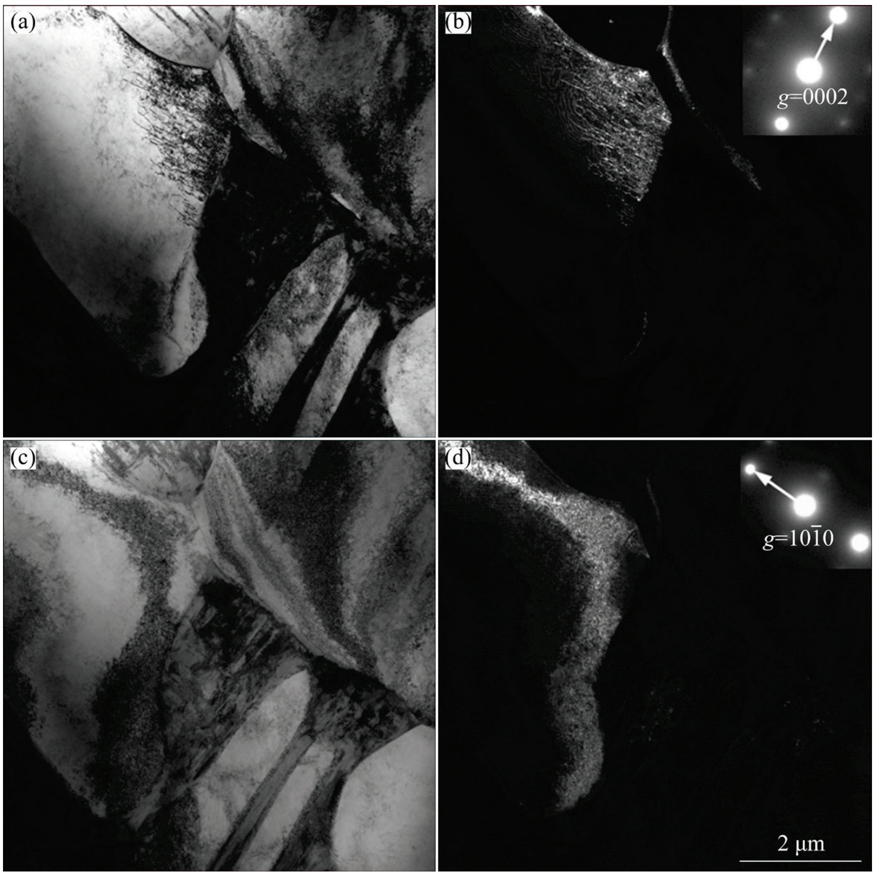


**Fig. 13** Dislocation morphologies of tensile fracture of alloy annealed at 800 °C: (a) Bright-field image of dislocations in $\alpha_p$ phase; (b) Dark-field image of same area shown in (a); (c) Bright-field image of dislocations in $\alpha_p$ phase; (d) Dark-field image of same area shown in (c)

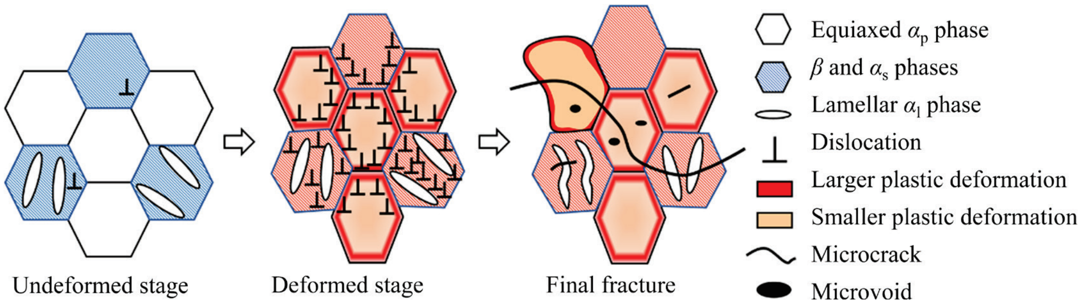


**Fig. 14** Schematic diagram of tensile fracture mechanism of Ti−6Al−4V alloy

## 4 Conclusions

(1) The as-forged microstructure is composed of equiaxed $\alpha_p$ and $\beta_t$ phases. The microstructure with annealing treatment below $T_\beta$ is similar to the as-forged microstructure. Meanwhile, all micro-structures have no obvious texture and the crystal orientation distribution is uniform.

(2) With the increase of annealing temperature, tensile strength increases first and then decreases, but the ductility has no significant fluctuation. It is found that strength and ductility are best matched under 860 °C, 1 h, AC condition, in which UTS= 1041 MPa, YS=937.7 MPa, EL=16.0%, and RA=45.6%, respectively. It can be ascribed to the combined action of a larger content of fine lamellar $\alpha_s$ phase.

(3) Fracture has typical ductile fracture mode for annealed samples due to the dominated dimples. The characteristics of microcracks, microvoids, and kinked $\alpha_p/\alpha_l$ phase are found near the fracture.

### CRediT authorship contribution statement

**Shi-shuang LIU:** Investigation, Conceptualization, Methodology, Experiment, Data curation, Writing − Original draft; **Jian-ming CAI:** Resources (material), Conceptualization, Writing − Review & editing; **Yi ZHOU:** Funding acquisition, Writing − Review & editing; **Jing-xia CAO:** Methodology, Funding acquisition; **Wang-feng ZHANG:** Formal analysis, Data curation, Writing − Review & editing; **Sheng-long DAI:** Funding acquisition; Supervision; **Xu HUANG:** Supervision, Resources, Writing − Review & editing; **Chun-xiao CAO:** Supervision, Writing − Review & editing.

### Declaration of competing interest

The authors declare that they have no known competing financial interests or personal relationships that could have appeared to influence the work reported in this paper.

### Acknowledgments

The authors are grateful to the National Science and Technology Major Project, China (Nos. 2017-VI-0004-0075, J2019-VI-0005-0119), Independent Innovation Special Fund Project of AECC (No. CXPT-2019-030), Stability Program for Basic Materials Research Institutes, China (Nos. 2019-0C-4753, CXPT-2020-033), and Fundamental Strengthening Program of AECC (No. 2021-JCJQ-JJ-0114) for financial support.

### References

[1] SHAHMIR H, LANGDON T G. Using heat treatments, high-pressure torsion and post-deformation annealing to optimize the properties of Ti−6Al−4V alloys [J]. Acta Materialia, 2017, 141: 419−426. https://doi.org/10.1016/j.actamat.2017.09.018.

[2] PENG He-li, LI Xi-feng, CHEN Xu, JIANG Jun, LUO Jing-feng, XIONG Wei, CHEN Jun. Effect of grain size on high-temperature stress relaxation behavior of fine-grained TC4 titanium alloy [J]. Transactions of Nonferrous Metals Society of China, 2020, 30(3): 668−677. https://doi.org/10.1016/S1003-6326(20)65244-X.

[3] LIU Xue-yan, LI Hong-wei, ZHAN Mei, ZHANG Hong-rui. Quantitative characterization of lamellar α precipitation behavior of IMI834 Ti-alloy in isothermal and non-isothermal heat treatments [J]. Transactions of Nonferrous Metals Society of China, 2022, 32: 162−174. https://doi.org/10.1016/S1003-6326(21)65785-0.

[4] LIU Shi-shuang, CAO Jing-xia, ZHOU Yi, HOU Chen-rui, DAI Sheng-long, HUANG Xu. Microstructure evolution and mechanical properties of a high-strength $Ti_2AlNb$ alloy processed by large-strain two-pass hot extrusion [J]. Journal of Alloys and Compounds, 2022, 925: 166715. https://doi.org/ 10.1016/j.jallcom.2022.166715.

[5] NATH P, MARANDI L, SEN I. Processing-microstructure-property correlation in thermo-mechanically processed Ti−6Al−4V alloys: A comparative study between conventional and novel approaches [J]. Journal of Alloys and Compounds, 2022, 927: 167039. https://doi.org/10.1016/j.jallcom.2022.167039.

[6] CHONG Yan, BHATTACHARJEE T, TIAN Yan-zhong, SHIBATA A, TSUJI N. Deformation mechanism of bimodal microstructure in Ti−6Al−4V alloy: The effects of intercritical annealing temperature and constituent hardness [J]. Journal of Materials Science & Technology, 2021, 71: 138−151. https://doi.org/10.1016/j.jmst.2020.08.057.

[7] JIA M T, ZHANG D L, GABBITAS B, LIANG J M, KONG C. A novel Ti−6Al−4V alloy microstructure with very high strength and good ductility [J]. Scripta Materialia, 2015, 107: 10−13. http://dx.doi.org/10.1016/j.scriptamat.2015.05.008.

[8] WANG Jian, LIN Xin, WANG Meng, LI Jia-qiang, WANG Chong, HUANG Wei-dong. Effects of subtransus heat treatments on microstructure features and mechanical properties of wire and arc additive manufactured Ti−6Al−4V alloy [J]. Materials Science and Engineering A, 2020, 776: 139020. https://doi.org/10.1016/j.msea.2020.139020.

[9] XU Jian-wei, ZENG Wei-dong, ZHOU Da-di, HE Sheng-tong, JIA Run-chen. Evolution of coordination between $\alpha$ and $\beta$ phases for two-phase titanium alloy during hot working [J]. Transactions of Nonferrous Metals Society of China, 2021, 31(11): 3428−3438. https://doi.org/10.1016/S1003-6326(21)65740-0.

[10] SINGH A P, YANG Fei, TORRENS R, GABBITAS B. Solution treatment of Ti−6Al−4V alloy produced by consolidating blended powder mixture using a powder compact extrusion route [J]. Materials Science and Engineering A, 2018, 712: 157−165. https://doi.org/10.1016/j.msea.2017.11.098.

[11] CHEN Zhao-qi, XU Li-juan, CAO Shou-zhen, YANG Jian-kai, ZHENG Yun-fei, XIAO Shu-long, TIAN Jing, CHEN Yu-yong. Characterization of hot deformation and microstructure evolution of a new metastable $\beta$ titanium alloy [J]. Transactions of Nonferrous Metals Society of China, 2022, 32(5): 1513−1529. https://doi.org/10.1016/S1003-6326(22)65890-4.

[12] YU Fei-long, ZHANG Yun, KONG C, YU Hai-liang. Microstructure and mechanical properties of Ti−6Al−4V alloy sheets via room-temperature rolling and cryorolling [J]. Materials Science and Engineering A, 2022, 834: 142600. https://doi.org/10.1016/j.msea.2022.142600.

[13] DAVARI N, ROSTAMI A, ABBASI S M. Effects of annealing temperature and quenching medium on microstructure, mechanical properties as well as fatigue behavior of Ti−6Al−4V alloy [J]. Materials Science and Engineering A, 2017, 683: 1−8. http://dx.doi.org/10.1016/j.msea.2016.11.095.

[14] ETESAMI S A, FOTOVVATI B, ASADI E. Heat treatment of Ti−6Al−4V alloy manufactured by laser-based powder-bed fusion: Process, microstructures, and mechanical properties correlations [J]. Journal of Alloys and Compounds, 2022, 895: 162618. https://doi.org/10.1016/j.jallcom.2021.162618.

[15] LIU Zheng, ZHAO Zi-bo, LIU Jian-rong, WANG Qing-jiang, GUO Zheng-hua, LIU Ze-min, ZENG Yi-da, YANG Guang, GONG Shui-li. Effects of solution-aging treatments on microstructure features, mechanical properties and damage behaviors of additive manufactured Ti−6Al−4V alloy [J]. Materials Science and Engineering A, 2021, 800: 140380. https://doi.org/10.1016/j.msea.2020.140380.

[16] JHA J S, TOPPO S P, SINGH R, TEWARI A, MISHRA S K. Deformation behavior of Ti−6Al−4V microstructures under uniaxial loading: Equiaxed vs. transformed-$\beta$ microstructures. Materials Characterization, 2021, 171: 110780. https://doi.org/10.1016/j.matchar.2020.110780.

[17] LIU Yang, XU Huai-zhong, PENG Bin-yi, WANG Xiao-feng, LI Shu-xin, WANG Qun, LI Zhi-guo, WANG Yong-gang. Effect of heating treatment on the microstructural evolution and dynamic tensile properties of Ti−6Al−4V alloy produced by selective laser melting [J]. Journal of Manufacturing Processes, 2022, 74: 244−255. https://doi.org/10.1016/j.jmapro.2021.12.035.

[18] LU Y, ARISTIZABAL M, WANG X, PANG B, CHIU Y L, KLOENNE Z T, FRASER H L, LORETTO M H. The influence of heat treatment on the microstructure and properties of HIPped Ti−6Al−4V [J]. Acta Materialia, 2019, 165: 520−527. https://doi.org/10.1016/j.actamat.2018.12.025.

[19] SUN Sheng-di, ZONG Ying-ying, SHAN De-bin, GUO Bin. Hot deformation behavior and microstructure evolution of TC4 titanium alloy [J]. Transactions of Nonferrous Metals Society of China, 2010, 20: 2181−2184. https://doi.org/10.1016/S1003-6326(09)60439-8.

[20] TAO Zhi-jun, FAN Xiao-guang, YANG He, MA Jun, LI Heng. A modified Johnson−Cook model for NC warm bending of large diameter thin-walled Ti−6Al−4V tube in wide ranges of strain rates and temperatures [J]. Transactions of Nonferrous Metals Society of China, 2018, 28: 298−308. https://doi.org/10.1016/S1003-6326(18)64663-1.

[21] ZHANG Chang-jiang, JIANG Xi, LÜ Zhi-dan, FENG Hong, ZHANG Shu-zhi, XU Ying, HAYAT M D, CAO Peng. Effect of duplex aging on microstructure and mechanical properties of near-$\beta$ titanium alloy processed by isothermal multidirectional forging [J]. Transactions of Nonferrous Metals Society of China, 2022, 32(4): 1159−1168. https://doi.org/10.1016/S1003-6326(22)65863-1

[22] CHONG Yan, BHATTACHARJEE T, PARK M H, SHIBATA A, TSUJI N. Factors determining room temperature mechanical properties of bimodal microstructures in Ti−6Al−4V alloy [J]. Materials Science and Engineering A, 2018, 730: 217−222. https://doi.org/10.1016/j.msea.2018.06.019.

[23] ZHANG Ding-chang, WANG Le-yun, ZHANG Huan, MALDAR A, ZHU Gao-ming, CHEN Wei, PARK J S, WANG Jie, ZENG Xiao-qin. Effect of heat treatment on the tensile behavior of selective laser melted Ti−6Al−4V by in situ X-ray characterization [J]. Acta Materialia, 2020, 189: 93−104. https://doi.org/10.1016/j.actamat.2020.03.003.

[24] WU Chuan, ZHAN Mei. Effect of solution plus aging heat treatment on microstructural evolution and mechanical properties of near-$\beta$ titanium alloy [J]. Transactions of Nonferrous Metals Society of China, 2019, 29: 997−1006. https://doi.org/10.1016/S1003-6326(19)65008-9.

[25] MUTOMBO K, SIYASIYA C, STUMPF W E. Diffusional transformation in Ti6Al4V alloy during isothermal compression [J]. Transactions of Nonferrous Metals Society of China, 2019, 29: 2078−2089. https://doi.org/10.1016/S1003- 6326(19)65114-9.

[26] JIANG Yu-qiang, LIN Y C, JIANG Xing-you, HE Dao-guang, ZHANG Xiao-yong, KOTKUNDE N. Hot tensile

properties, microstructure evolution and fracture mechanisms of Ti−6Al−4V alloy with initial coarse equiaxed phases [J]. Materials Characterization, 2020, 163: 110272. https://doi.org/10.1016/j.matchar.2020.110272.

[27] XIAO Yi, LANG Li-hui, XU Wen-cai, ZHANG De-xin. Diffusion bonding of Ti−6Al−4V titanium alloy powder and solid by hot isostatic pressing [J]. Transactions of Nonferrous Metals Society of China, 2022, 32(11): 3587−3595. https://doi.org/10.1016/S1003-6326(22)66041-2.

[28] LV Ji-ming, LUO Kai-yu, LU Hai-fei, WANG Zhao, LIU Jia-jun, LU Jin-zhong. Achieving high strength and ductility in selective laser melting Ti−6Al−4V alloy by laser shock peening [J]. Journal of Alloys and Compounds, 2022, 899: 163335. https://doi.org/10.1016/j. jallcom.2021.163335.

[29] YU Fei-long, ZHANG Yun, KONG C, YU Hai-liang. High strength and toughness of Ti−6Al−4V sheets via cryorolling and short-period annealing [J]. Materials Science and Engineering A, 2022, 854: 143766. https://doi.org/10.1016/j.msea.2022.143766.

[30] MA Jian-kai, ZHANG Ya-shan, LI Jun-jie, CUI Ding-cong, WANG Zhi-jun, WANG Jin-cheng. Microstructure and mechanical properties of forging-additive hybrid manufactured Ti−6Al−4V alloys [J]. Materials Science and Engineering A, 2021, 811: 140984. https://doi.org/10.1016/j.msea.2021.140984.

[31] YANG Liu-qing, YANG Yan-qing. Deformed microstructure and texture of Ti6Al4V alloy [J]. Transactions of Nonferrous Metals Society of China, 2014, 24: 3103−3110. https://doi.org/10.1016/S1003-6326(14)63448-8.

[32] HUANG Chao-wen, ZHAO Yong-qing, XIN She-wei, ZHOU Wei, LI Qian, ZENG Wei-dong. Effect of microstructure on torsion properties of Ti−5Al−5Mo−5V−3Cr−1Zr alloy [J]. Materials Science and Engineering A, 2017, 682: 202–210. http://dx.doi.org/10.1016/j.msea.2016.11.049.

[33] LI Chao, ZHANG Xiao-yong, LI Zhi-you, ZHOU Ke-chao. Effect of heat treatment on microstructure and mechanical properties of ultra-fine grained Ti–55511 near $\beta$ titanium alloy [J]. Rare Metal Materials and Engineering, 2015, 44(2): 327−332. https://doi.org/10.1016/S1875-5372(15)30029-1.

[34] HU Ming, DONG Li-min, ZHANG Zhi-qiang, LEI Xiao-fei, YANG Rui, SHA Yu-hui. Effects of multi-pass drawing strain and heat treatment on microstructure, texture and mechanical properties of Ti−6Al−4V alloy [J]. Materials Science and Engineering A, 2019, 757: 70−83. https://doi.org/10.1016/j.msea.2019.04.087.

[35] CHEN Yu-yong, DU Zhao-xin, XIAO Shu-long, XU Li-juan, TIAN Jing. Effect of aging heat treatment on microstructure and tensile properties of a new $\beta$ high strength titanium alloy [J]. Journal of Alloys and Compounds, 2014, 586: 588−592. http://dx.doi.org/10.1016/j.jallcom.2013.10.096.

[36] LIAO Yu, BAI Jun-hua, CHEN Fu-wen, XU Guang-long, CUI Yu-wen. Microstructural strengthening and toughening mechanisms in Fe-containing Ti−6Al−4V: A comparison between homogenization and aging treated states [J]. Journal of Materials Science & Technology, 2022, 99: 114−126. https://doi.org/10.1016/j.jmst.2021.04.063.

[37] LI H, MASON D E, BIELER T R, BOEHLERT C J, CRIMP M A. Methodology for estimating the critical resolved shear stress ratios of $\alpha$-phase Ti using EBSD-based trace analysis [J]. Acta Materialia, 2013, 61: 7555−7567. http://dx.doi.org/10.1016/j.actamat.2013.08.042.

[38] LI Tian-le, WU Hui-ping, WANG Bin, LI Sheng, LI Xi-feng, CHEN Jun. Fatigue crack growth behavior of TA15/TC4 dissimilar laminates fabricated by diffusion bonding [J]. International Journal of Fatigue, 2022, 156: 106646. https://doi.org/10.1016/j.ijfatigue.2021.106646.

[39] MATSUDA M, ANDO S, NISHIDA M. Dislocation structure in rapidly solidified $Mg_{97}Zn_1Y_2$ alloy with long period stacking order phase [J]. Materials Transactions, 2005, 46(2): 361−364. https://doi.org/10.2320/matertrans.46.361.

# 退火温度对多向锻造 Ti–6Al–4V 合金显微组织演变和拉伸行为的影响

刘石双，蔡建明，周 毅，曹京霞，张旺峰，戴圣龙，黄 旭，曹春晓

中国航发北京航空材料研究院 先进钛合金重点实验室，北京 100095

**摘 要**：为调节 Ti−6Al−4V 锻件显微组织和力学性能，进行一系列退火处理。结果表明：锻态和退火态组织均呈现由等轴初生 $\alpha$ 相($\alpha_p$)和转变 $\beta$ 相($\beta_t$)组成的双态组织。随着退火温度的升高，次生 $\alpha$ 相($\alpha_s$)从 $\beta$ 相中析出。组织中没有明显的织构，晶体取向均匀分布。同时，强度呈先增大后减小的变化趋势，而塑性没有明显的变化。在 860 ℃退火处理时，由于析出的细小 $\alpha_s$ 相含量较高，合金具有强度和塑性的良好匹配。所有断口表面均包含大量韧窝，为典型的韧性断裂特征。在断口附近发现微裂纹、微孔洞和扭结 $\alpha_p/\alpha_l$ 相(等轴 $\alpha_p$ 相和片层 $\alpha$ 相)特征。

**关键词**：Ti−6Al−4V 锻件；退火温度；显微组织演变；次生 $\alpha$ 相；拉伸性能；韧性断裂

**(Edited by Xiang-qun LI)**